Aerodynamic Analysis of a Transport Aircraft with a Boundary Layer Ingesting Aft-Propulsor at Cruise Flight Conditions

Arne Stuermer* and Sebastian Spinner†
DLR Institute of Aerodynamics and Flow Technology, Braunschweig, Germany
Marco Trost ‡ and Rainer Schnell§
DLR Institute of Propulsion Technology, Koeln, Germany

The implementation of advanced propulsion systems to ensure aviation meets the increasingly stringent environmental and economic pressures is a key building block in the development of future transport aircraft. A promising technology is the utilization of boundary layer ingesting (BLI) propulsion concepts, which are seen to offer an improvement of the engine propulsive efficiency in tandem with a reduction of the overall aircraft wake dissipation losses. In a collaborative study between the DLR Institute of Aerodynamics and Flow Technology, the DLR Institute of Propulsion Technology and industrial partners, a comprehensive study of the potential of implementing BLI concepts for future single-aisle short-to-medium range transport aircraft has been conducted. The present paper presents the result of an overall aircraft aerodynamic study, in which an aft BLI propulsor, specifically designed for this particular application, is investigated in its installation on the tail of a single aisle aircraft configuration at cruise flight conditions. A detailed aerodynamic analysis is presented, with a focus on comparing the results achievable through various BLI engine modeling approaches, which include the use of a classical engine boundary condition, a body force model as well as a full representation of the fan and OGV stage in a uRANS simulation approach. In addition to the study of the mutual aerodynamic interactions between the airframe and propulsor, some key aspects of the highest fidelity uRANS simulation approach are also discussed.

Nomenclature

c_p	Pressure coefficient, [-]
$F_{x,y,z}$	Forces in the cartesian coordinate system
H	Channel height
m	Massflow, $[kg/s]$
Ma	Mach number
p_t	Total pressure, $[N/m^2]$
r, R	Radial position, Rotor radius
t	Time, $[s]$
v_z	Velocity component in z directions, $[m/s]$
x, y, z	Cartesian coordinate system positions

Symbols

α	Angle of attack
ψ	Blade azimuthal position
ρ	Density

Abbreviations

BLI	Boundary Layer Ingestion
CFD	Computational Fluid Dynamics
CROR	Contra-Rotating Open Rotor
FPR	Fan Pressure Ratio
DLR	German Aerospace Center
HTP	Horizontal Tailplane
NASA	National Aeroanutics and Space Administration
OGV	Outlet Guide Vane
RANS	Reynolds Averaged Navier Stokes
uRANS	Unsteady Reynolds Averaged Navier Stokes
UHBR	Ultra High Bypass Ratio
VTP	Vertical Tailplane

*Research Scientist, Transport Aircraft Branch
†Research Scientist, Transport Aircraft Branch
‡Research Scientist, Fan and Compressor Branch
§Research Scientist, Fan and Compressor Branch

I. Introduction

The implementation of advanced propulsion systems to ensure future transport aircraft meet the increasingly stringent environmental and economic pressures as well as a growing awareness of society with respect to the need for sustainability are essential for the aviation industry to remain a vital and integral industry serving societal and economic needs. To meet these challenges, a more holistic design process addressing the propulsion-airframe-integration design at the overall system level is becoming a necessity. The concept of boundary layer ingestion (BLI) promises reductions in fuel consumption and CO2 emissions for modern commercial transport aircraft,[1,2] through the coupled exploitation of engine propulsive efficiency improvements and a reduction of the overall aircraft wake dissipation losses. The concept has been around since the early post war era,[3] and was later further developed by Smith,[4] introducing metrics to quantify the theoretical performance gains.

In a collaborative study between the DLR Institute of Aerodynamics and Flow Technology, the DLR Institute of Propulsion Technology and industrial partners, a comprehensive study of the potential of implementing BLI concepts for future single-aisle short-to-medium range transport aircraft has been conducted. The present paper presents the result of an aerodynamic study, in which an aft BLI propulsor, specifically designed for this particular application, is investigated in its installation on the tail of a single aisle transport aircraft configuration at cruise flight conditions. A detailed aerodynamic analysis is presented, which compares the results utilizing a number of different BLI engine modeling approaches available in the DLR developed CFD code TAU, ranging from the highest fidelity representation of the fully geometrically modeled aft propulsor in a uRANS simulation, to the usage of a body force model as a more efficient but physically accurate representation of the fan and OGV, and finally to the simplest representation of the propulsor using classical engine in- and outflow boundary conditions.

II. Configuration and Operating Point Definition

In the frame of a research partnership between DLR and industrial partners, a reference short-to-medium range single aisle aircraft focus configuration was developed and modified as a testbed for the studies of a possible retrofit target for a tailcone-mounted fuselage BLI-ingesting aft propulsor. As such, the configuration under study here, shown in the form of an instantaneous result of the unsteady RANS simulation discussed in this paper in figure 1, is in the 150-seat single aisle aircraft class. Similar in concept to the NASA STARC-ABL aircraft configuration,[1] it retains the under-wing mounted engines, which serve both for propulsion as well as the energy source to drive the aft propulsor. The latter was integrated with only minor modifications to the immediate aft region of the tailcone, with no special shape adaptations done to the empennage region to optimize airflow into the engine. The sole modification is the omission of the horizontal tail-plane (HTP), which is expected to be modified into a T-tail configuration rather than the conventional design typical for the 737 or A320. This design choice is driven by the desire to avoid the impingement of the HTP wakes on the aft propulsor fan blades, which would introduce additional flow non-uniformity and lead to likely significant unsteady blade loading with adverse impacts on blade structural design requirements and propulsor noise emissions. For the studies conducted in the frame of this research, the HTP has been omitted completely at this stage to avoid the non-essential task of designing a representative T-tail for this aircraft.

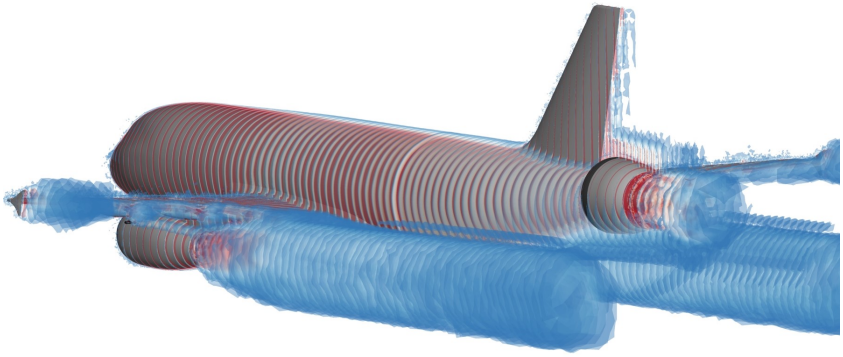

Figure 1. Instantaneous uRANS simulation results for the complete at cruise conditions

The aircraft is investigated in a cruise configuration and thus at an operating point in the flight envelope where the largest benefit of the efficiency gains through the BLI propulsor are expected, with a flight Mach number of $M = 0.79$ at an altitude of $h = 37000ft$, as listed in table 1.

	Ma	$\alpha[°]$	h [ft]
Cruise	0.79	1.8	37000

Table 1. Cruise flight condition specifications for the full aircraft analysis

For all simulations, the under-wing engines are retained in an identical baseline design and operating point, utilizing classical engine boundary conditions for the core and bypass engine exhaust and the fan face inlet.

II.A. Aft BLI-Propulsor Design

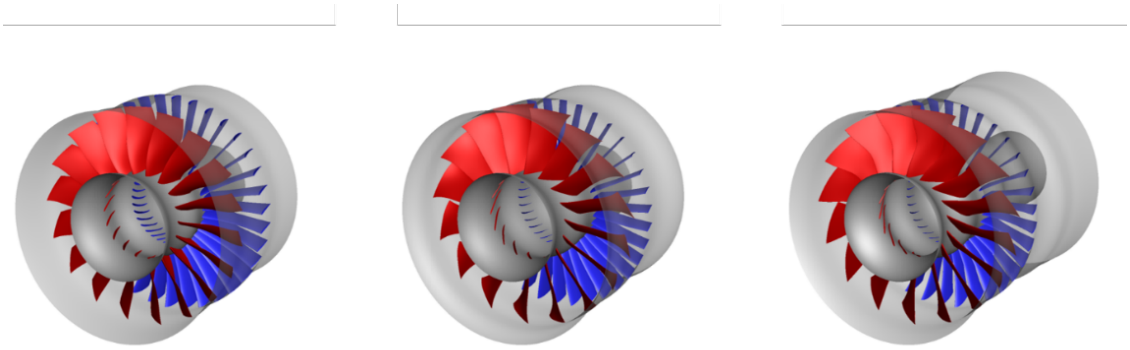

Figure 2. Isometric views of resulting aft propulsor geometries from all three design phases (not that the middle geometry stemming from phase 2 design iterations was used in the current study)

The aft propulsor used in the present study is a design created in cooperation with the DLR Institute of Propulsion Technology. The aft propulsor is a single-stage configuration consisting of rotor and OGV, operating at a target total pressure ratio of 1.26 and a mass flow rate of $236.8 kg/s$. Within the design process, several levels of design fidelity have been performed for the development of a highly efficient engine, specifically tailored to operate under BLI-like inflow conditions in a robust manner.
In a first approach, the aft propulsor was designed with homogeneous inflow conditions, as in case of clean inflow; this served as a baseline design and defined the achievable efficiency at benign inflow conditions. The design space was determined by the position and size of the nacelle. As part of the design process, a single passage through-flow optimization was performed with a Streamline-Curvature method (the ACDC solver,[5] coupled to the optimizer AutoOpti[6]) to generate the initial 3D blade and flowpath geometries for the subsequent 3D CFD calculations with 3D steady state CFD using DLR's TRACE solver.[7]

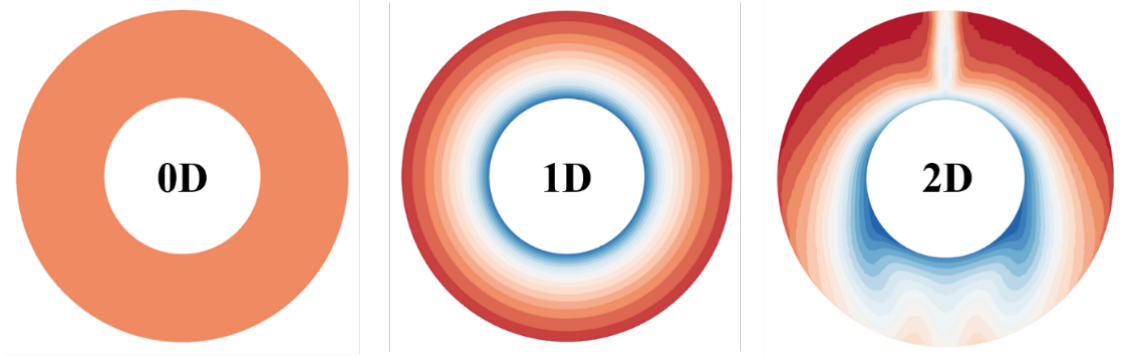

Figure 3. Engine inlet boundary conditions used during different stages of the propulsor design: constant inlet conditions (0D, left), circumferentially averaged, but radially varying conditions (1D, center) and full BLI profile (2D, right)

In a next step, 3D CFD single passage optimizations aiming maximum isentropic stage efficiency and ensuring sufficient surge margin of the aft propulsor design resulted in a final reference design with clean inflow (see figure 4, left). The actual geometry used in this paper is a result of a comparable 3D CFD single passage

optimization series, where the aerodynamic boundary inlet conditions were replaced with 1D inlet conditions. These inflow conditions, shown in the center of figure 3, were averaged using the 3D CFD results of the actual aircraft configuration as computed with TAU (see 3, right). This second aft propulsor design (see figure 4, center) shows a significantly improved performance in case of inlet flow distortion compared to the reference design for clean inflow.[8]

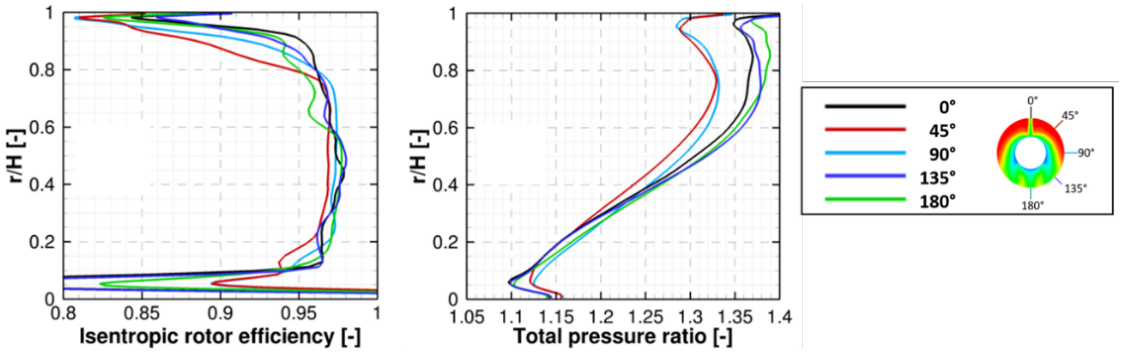

Figure 4. Example from phase 3 optimization studies: Different sectors used in a multi-sector RANS optimization (right) and resulting efficiency and pressure profiles in the different sectors (left)

In a third, multi-sector and RANS based design optimization phase, five CFD calculations with different mass weighted aerodynamic 1D inlet conditions to capture the most important inlet flow phenomena from the real 2D engine inlet front face (see figure 3, right and figure 4) were carried out to even better account for the circumferentially varying inlet conditions, resulting in a fully BLI compliant fan stage, the performance of which was verified in subsequent uRANS studies.
All resulting designs have comparable flow path distributions in common. In general, the hub and shroud lines show a reduction in the radial extent in the flow direction to align with the hub and tip lines of the outlet face of the nozzle geometry. Due to the unconventional design space, there is flow path diffusion in front of the blade areas of rotor and OGV to reach a flow path contraction within the blade areas itself. This stabilizes the flow field in the blade areas and accelerates the low energetic fluid in the hub regions to prevent flow separations.

III. Computational Strategy

All of the CFD computations discussed in this paper are performed using the DLR TAU-code,[9] an unstructured finite-volume vertex-based CFD solver developed by DLR. Spatial discretization of the convective fluxes is done using a second order central differencing scheme with matrix dissipation while the viscous fluxes are discretized with central differences. Turbulence in these fully turbulent simulations is modeled with the Wilcox k-ω model,[10] whereby the eddy viscosity is limited according to the Menter SST model.[11] For the uRANS simulations of the fully represented aft propulsor, the well-established dual time approach is used in the DLR TAU-code to compute unsteady flows.[12] For each discrete physical time step in a uRANS simulation a solution is obtained through a time-stepping procedure in a pseudo-time making use of the same convergence acceleration techniques used for steady-state computations, namely a lower-upper symmetric Gauss-Seidel (LU-SGS) implicit relaxation scheme, local time stepping, multigrid and residual smoothing.[13]
The simplest engine model utilized in these studies is the workhorse classical engine boundary condition, a 0D thermodynamic boundary condition based on averaged fan stage performance data. This boundary conditions requires the specification of the ratios of the total to the farfield static pressure and of the total to the farfield static temperature at planar surfaces representing the outlets of the engine. Alternatively a massflow of air along with the temperature ratio can be set here. Based on the specified values at the outlet, TAU computes the resulting engine jets in an iterative manned during the simulation. The inlet flow is either set through the specification of a massflow or it is determined through a coupling procedure with the outlets, which ensures that the massflow of air entering the engine through the inlet plane is equal to that being exhausted through the outlets.
The modeling of the engine with a body force model replaces the fan and OGV blades with volume specific source terms reproducing the blade forces imposed on the flow. The forces are smeared out in tangential direction, making for an azimuthally varying but steady-state representation of the unsteady turbomachinery

flow. No blade geometry is present in the computational mesh, but the model does benefit from a refined mesh close to the axial position that would be swept by the blade's leading and trailing edges. The reason for this are strong gradients in the source terms at these positions which need sufficient discretization.[14] As utilized in the TAU RANS simulations, the body force model is applied using a python interface and the Flowsimulator framework.[15] Flow data and source terms are exchanged between the solver and the body force model. After obtaining an initial solution, the flow state in the cells swept by the blades is communicated to the body force module. The body force model then computes source terms for the right hand side of the RANS equations representing engine performance. These source terms are then communicated back to the flow solver and added to the equations in the affected cells. The flow solver is then run for a user defined number of iterations until the body force module is called again. This loop is repeated until externally defined convergence criteria are met. Before performing the first simulation, the body force model is calibrated using performance data from the engine design process in the form of either 0D or 1D performance metrics. The computation of the source terms is done using Hall's model,[16] with modifications introduced by Thollet.[17–19]

For the uRANS approach, the fan and OGV blades are fully geometrically represented and modeled as viscous surfaces in the TAU simulations. This represents the present highest fidelity modeling of the installed aft propulsor on the aircraft, at the cost of the largest mesh size as well as the most costly and time-consuming simulation run-times. In order to simulate the relative motion of the rotor, use is made of the codes Chimera capability as well as the implemented motion libraries.[20,21]

All TAU simulations discussed in this paper share a common CFD setup. The computational domain was divided into several individual mesh blocks which are combined using the code's Chimera capability. This allowed the re-use of the aircraft meshes for the different TAU engine modeling approaches by only exchanging the fan/OGV stage meshes.

III.A. Mesh Generation

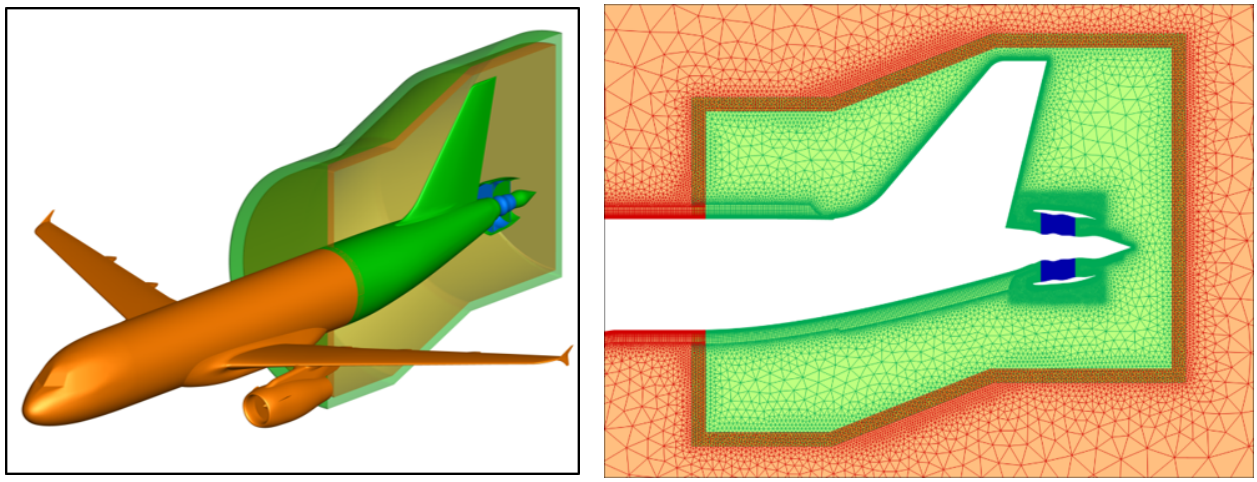

(a) Chimera blocking strategy for the complete aircraft

(b) Hybrid-unstructured aircraft empennage mesh

Figure 5. Chimera mesh blocking for the complete aircraft case

For the full aircraft simulations discussed here, the flexibility afforded by the Chimera approach was exploited and meshes consisting of three or four mesh blocks were created. The overall Chimera blocking setup is shown in figure 5(a). The first two mesh blocks, both of which are hybrid-unstructured CentaurSoft Centaur generated grids, are for the forward portion and the empennage region of the aircraft. This split was done to enable variations of the aft propulsor installation, accommodating small design adaptations of the nacelle for example, to be included without having to re-generate the entire aircraft mesh. A significant effort was devoted to ensuring a good mesh resolution in the fuselage up to the aft propulsor location was available. The prism or hex block layer created to ensure this is well visible in figure 5(b). Embedded in the empennage mesh block are the grids required to account for the BLI propulsor, in an embodiment as required for the specific modeling approach. For the body force modeling for example, one additional mesh block is needed in the volume enclosing the rotor and OGV blades, which is shown in blue in figure 5(b).

In the uRANS approach one mesh block each for the rotor and the stator of the BLI propulsor fan stage are required. The fan stage meshes are block-structured grids generated using the commercial ANSYS ICEM CFD Hexa mesh generation software. In addition to ensuring an adequate resolution of boundary layers (including the laminar sublayer) on all surfaces of the aircraft and propulsor, another essential aspect of the rotor meshing approach relates to the need to ensure the transfer of the fan blade wakes into the stator mesh blocks is possible in the uRANS simulation with minimal interpolation losses.[22] Thus, the overlap region of the front and aft rotor grids is meshed in a way that ensures an identical, axially-aligned cell orientation, and a matching number and uniform spacing of the cells for the annulus on the rear Chimera boundary of the rotor and the forward Chimera boundary of the OGV. As shown in figure 6(b), the mesh features a total of 1632 cells in azimuthal direction at the rotor-rotor interface on either side.

For all mesh blocks the symmetry or axisymmetry of the various geometric components was exploited where

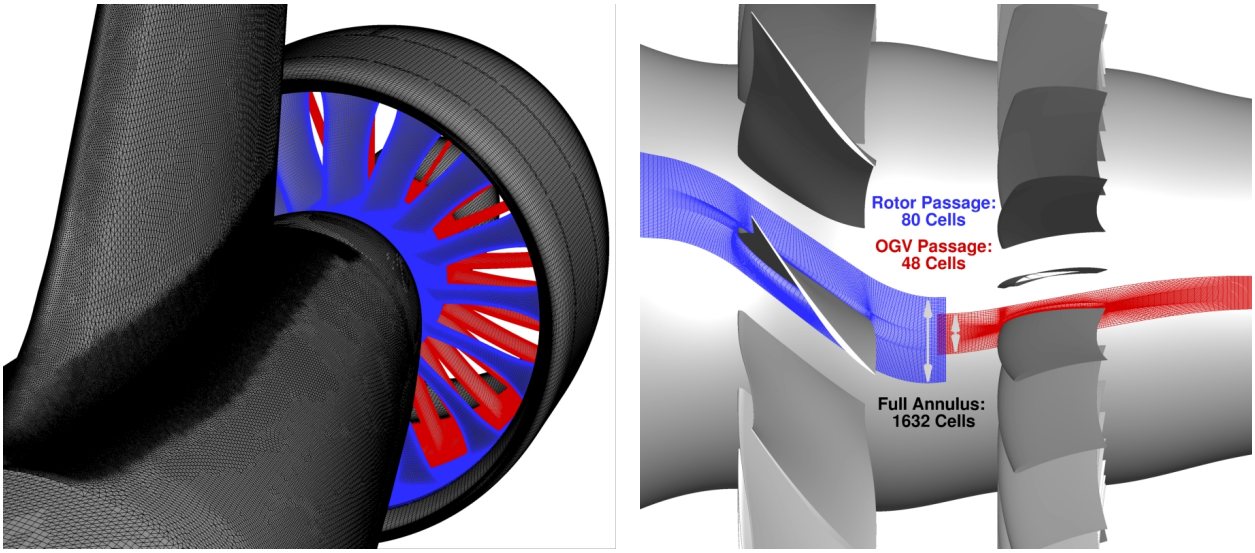

(a) Empennage region surface mesh details

(b) Rotor-stator interface region meshing

Figure 6. Chimera mesh blocking for the installed tail-mounted propulsor uRANS simulation

possible, ensuring, for example, that each blade of the rotor and OGV has a common spatial discretization. An overview of the mesh parameters is listed in table 2.

	Aircraft	Empennage	Fan	OGV	Total
Complete Aircraft, uRANS	90.5e6	21.9e6	32.9e6	31.1e6	176.5e6
Complete Aircraft, Body Force	90.5e6	21.9e6	10.6e6		122.9e6
Half Aircraft, Engine BC	45.3e6	11e6	1.9e6		58.2e6

Table 2. Chimera mesh size overview

III.B. The uRANS Simulation Approach

The engine boundary condition and body force model simulations are relatively straight-forward steady-state RANS runs, where mainly the various iteration approaches between the external flow and the model for the BLI propulsor are specific features, which operate as described above. The uRANS simulation approach for the complete aft propulsor aircraft configuration builds on experience gained in the recent past on similar studies on the propulsion-airframe integration for CROR and UHBR engines.[22–25] In this approach, the computations are initialized with a steady-state simulation in which the rotors remain stationary. In the subsequent unsteady simulation, a step-by-step refinement of the time-step size is performed, with the aim of studying the impact of the temporal resolution on the aerodynamic results, in particular the fan-OGV interactions.

Table 3 lists the various temporal resolutions in terms of the number of time steps per rotor revolution for which solution output is obtained and analyzed. The final and smallest time-step per mesh is linked to the

	Δt_1	Δt_2	Δt_3	Δt_4	Δt_5	Δt_6
Complete BLI-Aircraft uRANS	90p	180p	360p	720p	1440p	1632p

Table 3. Computational matrix in terms of temporal resolutions studied

mesh resolution at the rotor-rotor Chimera interface. It corresponds to a deflection of the rotor for which there is only a one cell relative motion between the fan and OGV. Thus, for the fan stage mesh setup as shown in figure 6(b), the highest temporal resolution studied called for 1632 time steps per rotation, i.e. a rotor motion of $\Delta\Psi/\Delta t = 0.221°$ per physical time step.

IV. Aerodynamic Analysis

The integration of the aft propulsor on the tailcone of the aircraft, while drawing the efficiency benefit associated to the ingestion of the fuselage boundary layer around the full annulus of the propulsion system also leads to several notable sources of unsteady loading for a fan blade during its rotation. For an individual fan blade during one complete rotation, the flowfield exhibits strong unsteady phenomena which are periodic in nature in the rotating reference frame. Therefore it is convenient to refer to a blade or rotor azimuthal position during the rotation of the fan. The azimuthal position is based on a reference blade position for the rotor, the definition of which is included in figure 7, which shows the fan disc loading as a results of the uRANS simulation at the highest temporal resolution. The initial position, the angle of $\Psi = 0°$, is defined as corresponding to the reference blade pointing upwards along the z-axis and increases in the direction of the fan sense of rotation.

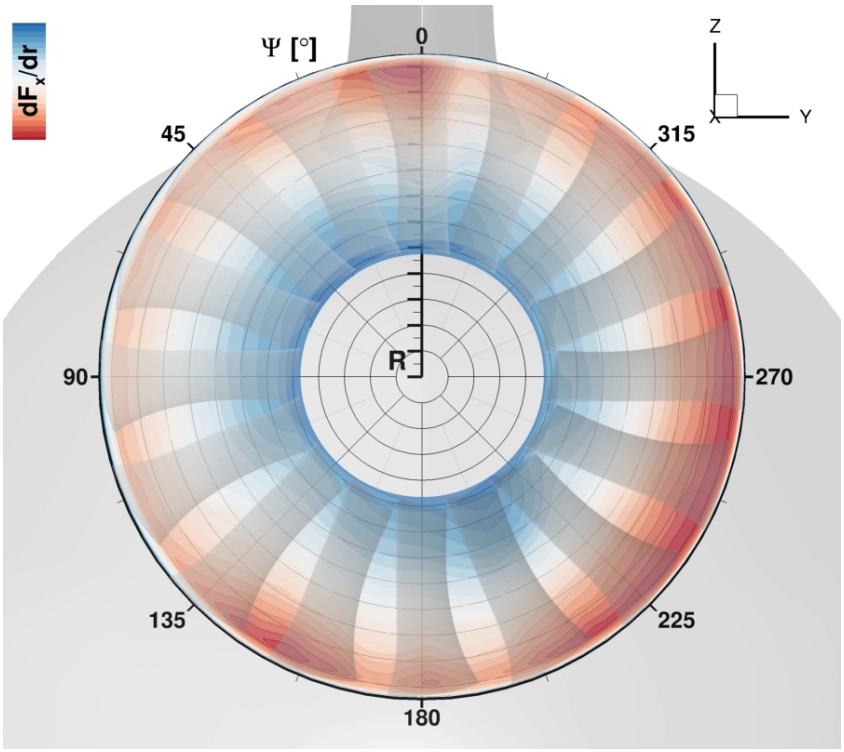

Figure 7. Inflow non-uniformity impact on fan blade axial force disc loading for the aft propulsor rotor

Figure 8(a) shows regions of reduced total pressure, with a focus on the axial position of the BLI propulsor inlet, to identify the main inflow distortions ingested by the engine. One obvious non-uniformity for the fan inflow is caused by the wake of the vertical tail plane (VTP). As can be seen in the visualization of the total pressure losses at several axial locations along the aircraft empennage in figure 8(b), this leads to a region of low-velocity flow impinging on the blades at an azimuthal position of $\Psi = 0°$. The associated blade response is visible in the plot of the fan axial force loading across the fan plane in figure 7. This shows that the radial load is increased around this azimuthal position, in line with the fan blade effective angle of attack increase the VTP wake introduces to the inlet flow here. The most pronounced loading increase is seen in the tip region of the fan blade.

The flow structures visualized in figures 8(a) and 8(b) show that additional sources of flow non-uniformity for the fan inflow are caused by vortices that emanate from both the upper and the lower side of the wing at its junction with the fuselage. Figures 8(a) and 8(b) show a small trailing edge separation region on the wing trailing edge upper surface at the intersection with the fuselage. This perturbed flow then forms

vortices, which are convected from the wing root along the empennage underside into the aft propulsor nacelle, interacting with the blades of the fan as it passes the azimuthal positions $\Psi = 135°$ and $\Psi = 225°$. The fan disc loading in figure 7 shows notable axial loading fluctuations for this region of the annulus due to these blade-vortex interactions. A notable vortex also forms on the underside of the wing, beginning at the slat horn/leading edge of the wing shown in figure 8(c). This vortex is also convected along the empennage underside from both sides of the fuselage and joins at the centerline to form the inflow perturbation that leads to unsteady blade loadings, in particular at the blade tips, at $\Psi = 180°$.

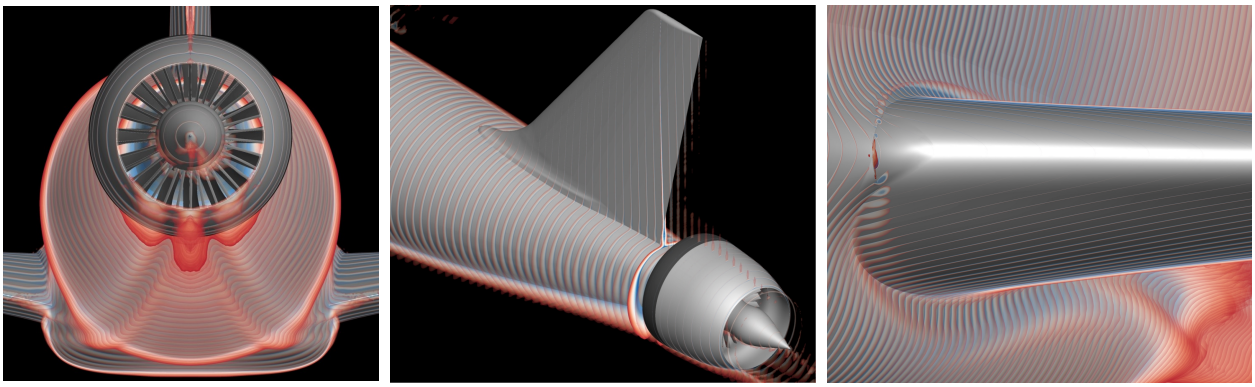

(a) BLI Propulsor inflow perturbations (b) Empennage region flow features (c) Slat horn and wing root vortices

Figure 8. Instantaneous uRANS simulation result showing sources of inflow distortion for the BLI aft propulsor

IV.A. uRANS Simulation Analysis

The uRANS simulation approach in focus in the frame of this study, accounting for the full range of installation effects present for the aft BLI propulsor, allows for an in-depth analysis and understanding of the effect these inflow perturbations have on the unsteady loading of the individual rotor and OGV blades and the fan stage as whole.

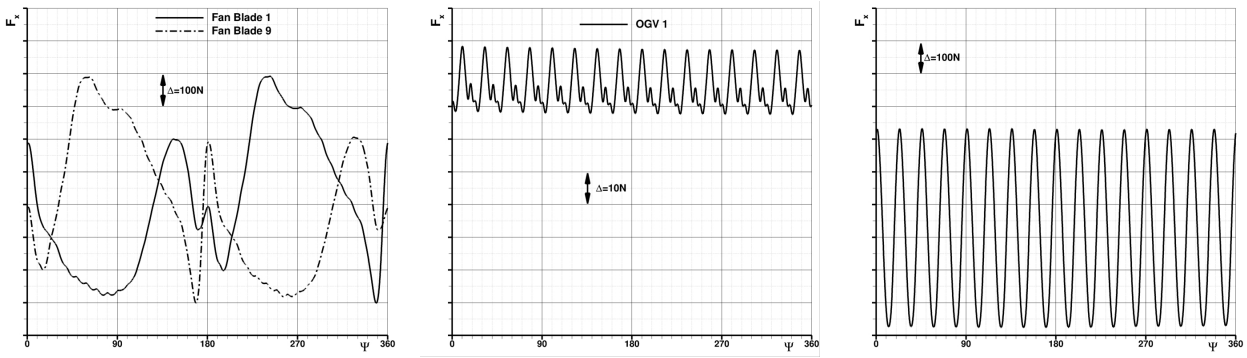

(a) Reference fan blade axial force (b) Top OGV blade axial force (c) Rotor axial force development

Figure 9. Fan stage axial force time history for one rotor revolution at the highest uRANS temporal resolution

Figure 9 shows the axial/thrust force time histories during one complete revolution of the rotor - using the azimuth definitions as described for figure 7 - as taken from the uRANS simulation result at the highest temporal accuracy. For an individual rotor blades full axial force development shown in figure 9(a), the key impact of the VTP wake as well as the vortical flow features convected along the empennage from the wing upper and lower wing surfaces are in line with the description given with respect to figure 7. Here, the abrupt impact of the VTP wake leading to increased blade loadings as well as the generally more gradual loading increase and decrease across a greater azimuthal range due to the interaction with the vortices is clearly evident for the reference blade. For comparison, the dash-dotted line in figure 9(a) for the diametrically opposed blade 9 of the rotor indicates that an excellent degree of periodicity has has been obtained in the

uRANS simulation.
When evaluating the rotor as a whole, figure 9(c) shows that here a 16-cycle unsteady loading is present in the axial forces. The amplitude is just slightly smaller than seen for the individual blades, but clearly shows that each blades 1P-loading due the inflow perturbations also dominates the rotor unsteady loading.
Representative for all of the individual outlet guide vanes, which differ mainly in the mean loading across the azimuth, figure 9(b) shows the axial force time history for the top/12 oclock oriented OGV number 1. This shows an unsteady loading that is an order of magnitude less than for the rotor blades, and is the results of the interaction with the blade wakes generated by the latter as they pass in front of the vane 16 times during one rotor revolution.

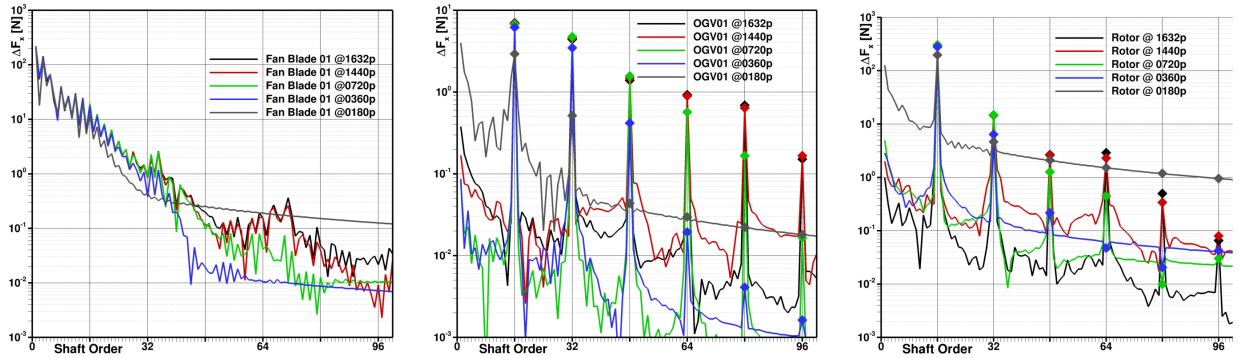

(a) Reference fan blade axial force unsteady loading (b) Top OGV blade axial force unsteady loading (c) Rotor full wheel axial force unsteady loading

Figure 10. Fan stage axial force spectral analysis in dependence of uRANS temporal resolution

The accurate resolution of these unsteady interactions between the rotor and OGV as well as the inflow perturbations on the rotor is strongly dependent on the temporal resolution used in the uRANS simulation. Figure 10 plots the spectral analysis of the reference fan and OGV blade unsteady axial force loadings (as seen in figures 9(a) and 9(b) respectively), as a function of the shaft order for the time step refinement study performed. An analagous unsteady loading analysis for the full wheel of the rotor is shown in figure 10(c).
For the fan blade, figure 10(a) reveals that for all but the highest harmonics of the fundamental loading cycle at shaft order 1, time step refinement does not impact the quality of the key 1P-loading cycle predictions too much. Mainly the coarse temporal resolution of 180p, which resolves the rotor revolution using 180 time steps, shows some notable deviations even at lower frequencies, while the 360p resolution is only notably different at the higher frequencies. For the full wheel of the rotor, figure 10(c) echoes these findings, showing that the 1P loading cycle amplitude - which manifests at shaft order 16 at the rotor level - is only underpredicted at the coarsest time-step of 180p. Higher harmonics thereof show an essentially good match for the two highest temporal respolutions, with deviatins to these becoming larger as the time step size is increased.
For the OGV reference blade results plotted in figure 10(b), the 180p resolution is seen to be too coarse to resolve the amplitude of the fundamental loading cycle at shaft order 16. The 360p time step size shows an amplitude prediction offset versus the higher temporal resolutions beginning at the first harmonic of the fundamental loading . The two highest temproal resolutions of 1440p and 1632p are seen to give unsteady loading predictions that are in very good agreement up to the fifth harmonic included in the figure.
Thus, in conclusion, while a coarse time step size of around 360p seems to be sufficient to resolve a good representation of the rotor unsteady loading, if a high degree of fidelity in the OGV unsteady loading is a key metric to be determined in the uRANS simulations, a temporal resolution of greater than 0720p is required. This is equivalent to using more than 45 time steps - with the 1440p resolution thus 90 time steps - to resolve the key periodic unsteady loading due to the interaction with the rotor blade wakes.
As found in previous research,[22–25] the predicition of the key mean performance metrics is less dependent on the temporal resolution used in the uRANS simulation. The overall fan pressure ration (FPR) and the mass flow rate through the aft propulsor are two of the main performance measures in focus in this study. For convenience, both of these values are evaluated using the Chimera boundaries, as shown in figure 11(a). The mass flow rate, evaluated both at the fan inflow and OGV outflow stations, is determined through an integration of the mass flow rate through these surfaces using an averaged state from one complete rotor

revolution at the various time step sizes. The FPR results from a similar approach, using the averaged total pressures on the OGV outflow and the fan inflow planes.
Figure 11(b) shows the uRANS results for the FPR as a function of the number of time steps used to resolve one rotor revolution. A general trend of convergence to a value of 1.2628 can be seen as the time step is refined, but the difference between this value and that found for the 0180p temporal resolution is small at just under 0.2%. The deviation of the TAU uRANS prediction to the design spec value of 1.26 is again quite small at just over 0.2%.

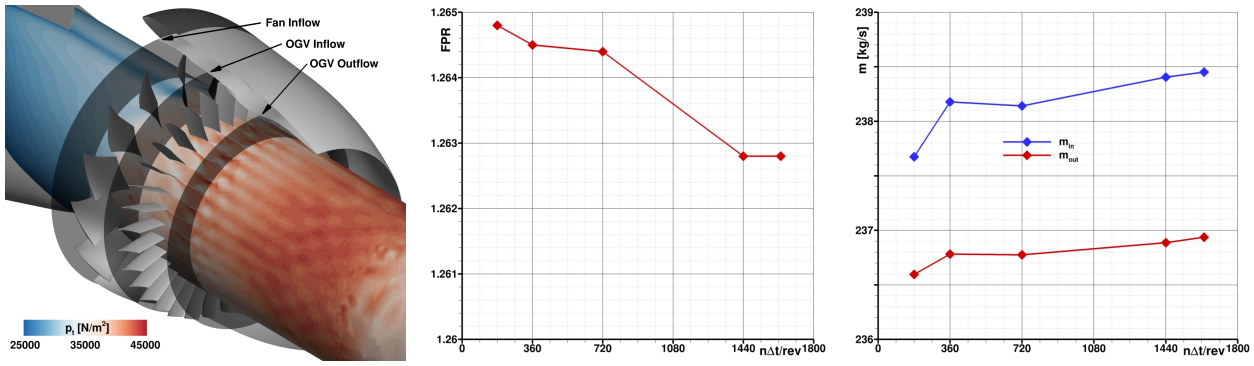

(a) Station definitions (b) Overall fan pressure ratio (c) In- and outlet massflow rates

Figure 11. uRANS mean performance predicitions in dependence of temporal resolution

Figure 11(c) plots the uRANS results for the mass flow rate through the fan inflow and the OGV outflow Chimera interface as a function of the number of time steps used to resolve one rotor revolution. The Chimera boundary condition in TAU is non-conservative, and therefore a small difference in the massflows as they pass through the fan in- and outflow and the OGV in- and outflow boundaries is not unexpected. This can be seen to result in a roughly 0.6% difference in the overall fan stage in- and outflow massflows in figure 11(c) for all temporal resolutions. While clearly not the ideal method to predict turbomachinery performance in the tight margins expected for today's dedicated design codes, for the application here, where the overall performance of the propulsion-airframe system is the focus, this relatively small massflow offset is not viewed as a detriment to the study. Both the in- and outlet massflows show a convergence trend with time step refinement. Again, the temporal resolution dependence is small, with the largest discrepancy between the inlet massflow at 0180p and 1632p amounting to no more than 0.3%. The match of the outlet massflow to the design spec is within 0.1% in all cases. Thus, mean performance predictions for the aft BLI propulsor in the installed setting are seen to be possible with a high degree of confidence and accuracy without a notable temporal resolution dependence, making coarse time-step uRANS runs with relatively modest run-times a feasible and valuable approach to gauge the performance of these engine-airframe installations.

IV.B. BLI Propulsor Modeling Comparison

The uRANS simulation approach, including a full geometrical modeling of the BLI propulsor, is expected to be the highest fidelity approach to fully account for all of the complex mutual interactions that occur between the airframe and tightly integrated propulsion system. While it was shown that good mean performance predictions are possible using this approach and relatively large time step sizes, which yield run-time for the uRANS analysis on the order of days (versus weeks, if the full unsteady nature of the flowfield is to be adequately accounted for), alternative engine modeling approaches for the BLI propulsor are available and may be the better choice for many of the analyses of interest due to significantly smaller meshes and shorter simulations times. Two additional models available in the DLR TAU code are studied for this aircraft configuration also. The aft BLI propulsor mean performance results for the highest temporal resolution uRANS simulation, a CFD analysis using a body force model as well as one applying the simplest engine boundary condition are summarized in table 4.
With the uRANS results having been discussed in the previous section, a favorable comparison with the body force predictions is evident in the data. the difference between the in- and outflow massflows between the uRANS and the body force simulations is less then 0.7% and 0.4% respectively. For the body force model, the massflow rate through the engine is in near perfect agreement with the specs of $236.8 kg/s$. As

the Chimera methodology is also applied to embed the body force model optimized mesh block into the empennage region, a small impact of the non-conservative nature of that boundary condition is also seen here. The FPR is also in near-perfect agreement with the engine design spec of 1.26, and shows just an 0.1% to the mean uRANS predicition. For the simulation with the engine boundary condition, the massflow rate per design specs was specified as a constraint, which lead to the inlet and outlet plane static pressures being iterated to achieve that target value. Thus the FPR is the free parameter in that simulation, which results in a slight underprediction of around 0.2% versus the other cases.

	uRANS	Body Force	Boundary Condition
$m_{F,in}[kg/s]$	238.45	236.892	236.8
$m_{F,out}[kg/s]$	236.93	236.914	236.8
Chimera Loss	$1.52kg/s(0.6\%)$	$0.022kg/s(0.01\%)$	–
Overall FPR	1.2628	1.2610	1.2566

Table 4. Mean performance predictions for the BLI propulsor by the differing engine models

Differences in the predictions from the various modeling approaches do become more evident when looking at details of the aerodynamic results. A comparison in terms of the total pressure development in the empennage region and the flow through the propulsor are shown in figure 12. The left column shows total pressure contour plots on the horizontal plane through the propulsor from the highest temporal resolution uRANS, the body force model and the boundary condition simulations. Figure 12(a) is an instantaeous topßdown view snapshot from the uRANS run, and as such clearly shows the presence of total pressure fluctuations in axial direction due to the presence of the blade wakes as they are convected through the engine. In line with the higher rotor blade loadings seen on the left versus the right side of the rotor, the total pressures are also greater on that side of the flowpath here. Qualitatively in good agreement, the body force model results in figure 12(c) show the same trends in terms of azimuthal non-uniformity of the jet development, naturally without any of the unsteady flow characteristics such as blade wakes. The gradual increase in total pressure introduced in the volume of the flowpath enclosing the rotor and stator is nicely evident in the plot. Finally and in contarts to these results, the engine boundary condition solution total pressure contours in 12(e) show the inherent drawback of this model, when applied to engines that are subject to strong inflow non-uniformity. While both previous simulations account for the impact of that in terms of azimuthally varying blade loadings and thus jet development, the engine boundary condition applies a constant static or total pressure on the in- and outflow planes resepctively, negating any chance of properly representing the non-uniform exhaust stream. For all cases a rather abrupt decay of the engine jet is evident in the left side of each figure, coinciding with the Chimera boundary between the empennage and overall aircraft mesh block. This is due to the much coarser mesh of the overall aircraft mesh in this region, which was not set up to sustain the jet far downstream.

A quantitative comparison of radial total pressure profiles through the engine in the horizontal plane is shown in the right column of 12. Here the uRANS data is shown as a time averaged result for a direct comparison with the other two modeling approaches. The axial stations for this comparison, an intake, a nozzle and a jet location, are marked by the black lines shown in figure 12(c). For the intake radial profiles in figure 12(b), all three modeling approaches show a good match in in total pressure for most of the channel height. Merely in the tip region both the body force and boundary condition results show slightly lower values. Most likely the perturbation of the intake lip boundary layer in this region due to the periodic physical presence of a rotor blade just downstream and its displacement effect on the flow are the cause for this small difference. At the nozzle axial station, the clear outlier is the boundary condition result, which, true to the design of this model, yields an essentially constant total pressure for the full channel height and is identical on the left and right sides. The mean uRANS and the body force model result however do show a very good agreement qualitatively and quantitatively. For the inner portions of the channel height, the total pressure predictions are essentially identical, with deviations only evident in the tip region. An underprediction of the peak magnitude on the right side of the engine at this station is the most notable offset between the two solutions. These observations and comparisons between all three results hold also for the jet axial location in figure 12(f), with all results alos clearly showing the mixing out of the jet with the surrounding flow. Again, the most notable difference between the mean uRANS and the body force model result is the underprediction of the peak magnitude in total pressure on the right side of the propulsor.

This analysis indicates that save for some small details all three modeling approaches yield comparable results in the intake of the propulsor, but only the uRANS and body force approaches are naturally capable to capture the proper flow physics in the jet development.

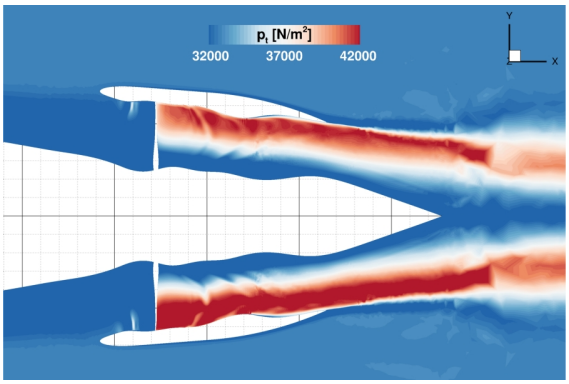

(a) uRANS instantaneous result

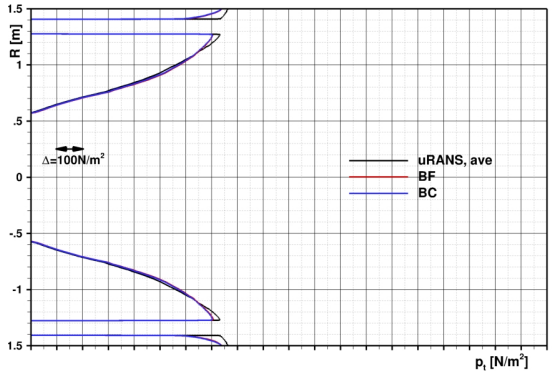

(b) Intake region total pressure profiles

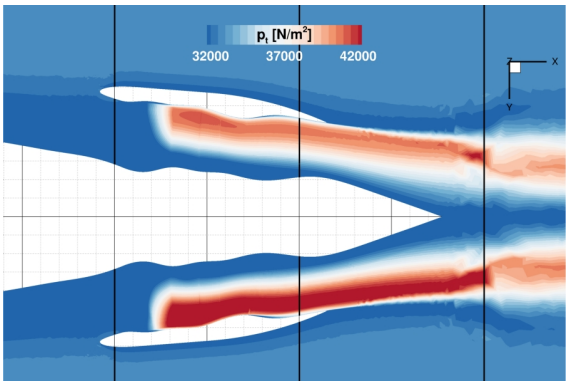

(c) Body Force Model result

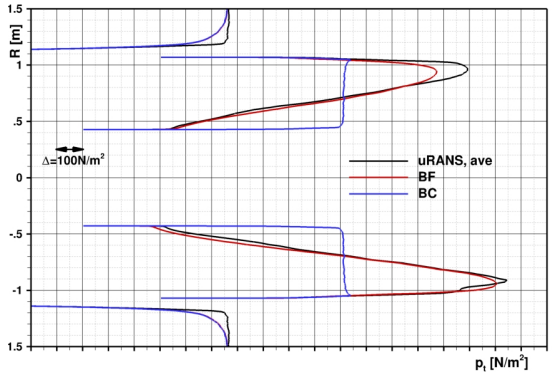

(d) Nozzle region total pressure profiles

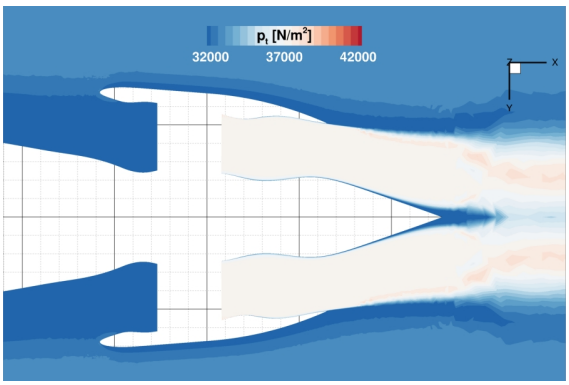

(e) Boundary Condition Model result

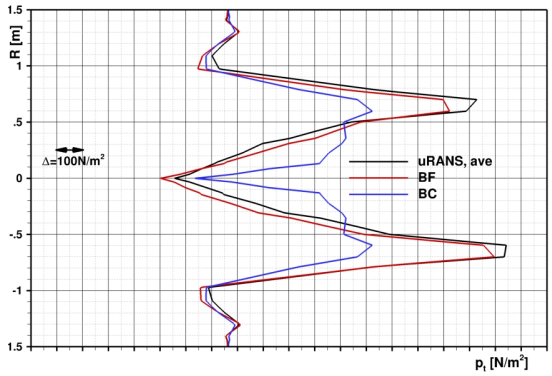

(f) Jet total pressure profiles

Figure 12. Comparison of BLI propulsor total pressure development predictions along the horizontal plane through the engine centerline. Axial locations for the total pressure profiles are marked as black lines in figure 12(c)

Figure 13 compares the aft propulsor nacelle pressure distributions for the three engine modeling approaches for the top, right, bottom and left side positions in figures 13(a), 13(b), 13(c) and 13(d) respectively. Again, the uRANS results are shown as time averaged data from one full rotor revolution at the highest temporal accuracy. Generally, the uRANS and the body force results show a very close agreement for all external portions of the nacelle as well as into the intake. In most cases, just a small underprediction of the suction peak levels at the intake lip is seen for the body force versus the uRANS results. The boundary condition results generally have an even slightly less pronounced intake lip suction peak, but do match the other data well on the outer portion of the nacelle. One notable offset is seen in the intake for the bottom nacelle section in figure 13(c), where slightly higher pressures, i.e. a lower flow acceleration, are predicted

by the boundary condition simulations in comparison to the other cases. Larger differences are seen for the nozzle and plug pressure distributions. On the plug, the boundary condition results reflect the impact of the constant total pressure distribution on the complete outlet plane, which leads to higher pressure values just downstream of the OGV outlet than is found in the other data. This is followed by a higher pressure gradient and flow acceleration through the nozzle. On the casing side of the nozzle, there is generally a better match between all three cases.

With the exception of some smaller deviations in the intake lip suction peak levels, all three modeling approaches thus show generally similar predictions for the external portions of the nacelle flowfield. Notable differences are found for the internal nozzle and plug pressure distributions, which reflect the small (uRANS versus body force) or large (boundary condition) differences in the engine exhaust stream modeling due to the different simulation approaches.

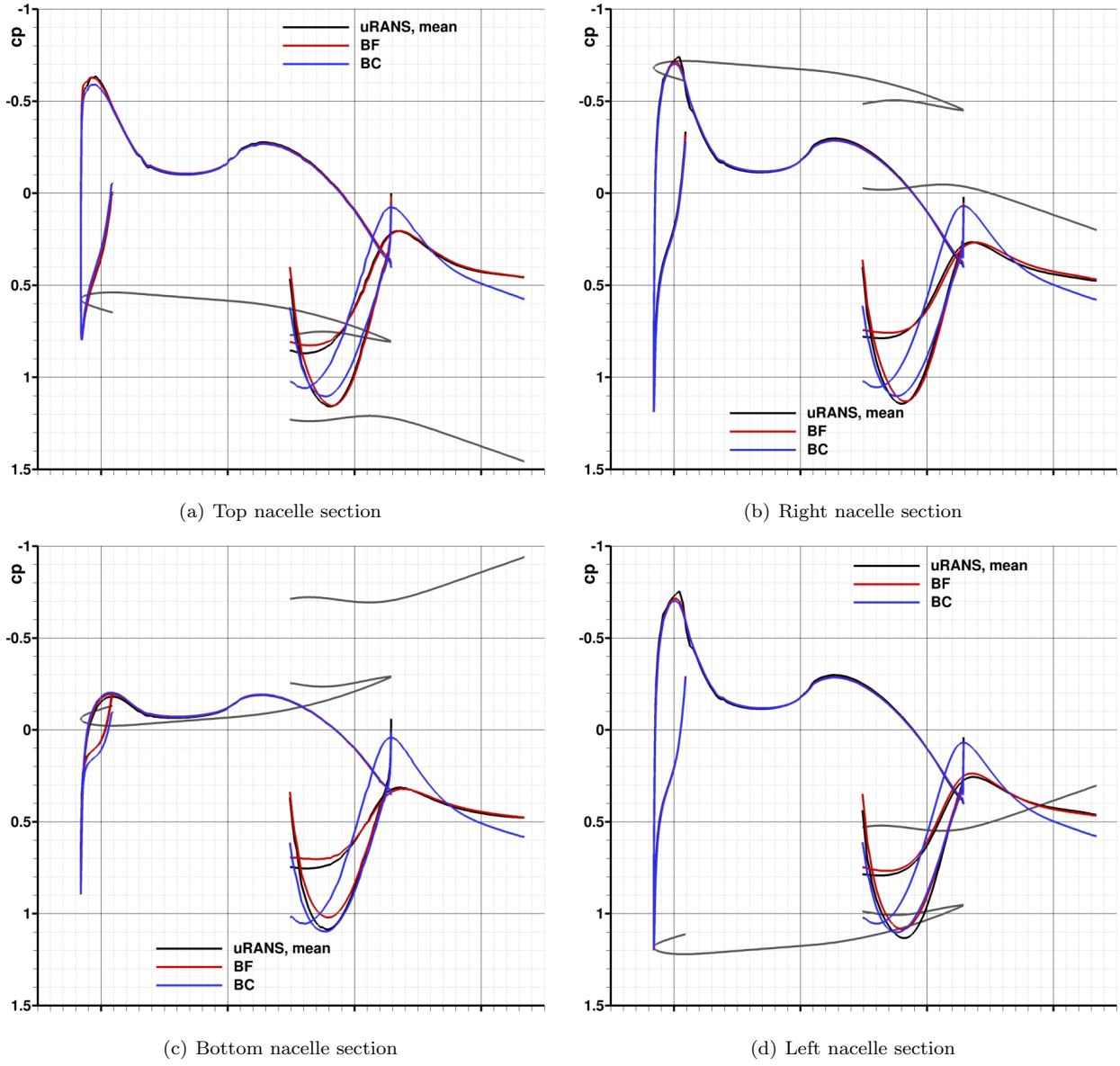

(a) Top nacelle section

(b) Right nacelle section

(c) Bottom nacelle section

(d) Left nacelle section

Figure 13. Nacelle pressure distribution comparison

More significant differences between all three engine modeling approaches are seen in an analysis of the swirl development through the engine, as plotted for two axial locations in the horizontal plane through the engine axis in figure 14. For the nozzle section in figure 14(b), there is no swirl component downstream of the OGV for the boundary condition modeling of the propulsor. This is as expected, since merely a static pressure prescription on an outlet plane is used to model the outlfow from the fan stage, thus no swirl losses can be

accounted for. The body force and the mean uRANS results indicate non-negligible swirl losses do occur, including, in the latter case, peaks in the velocity in the tip region indicative of the tip vortices.

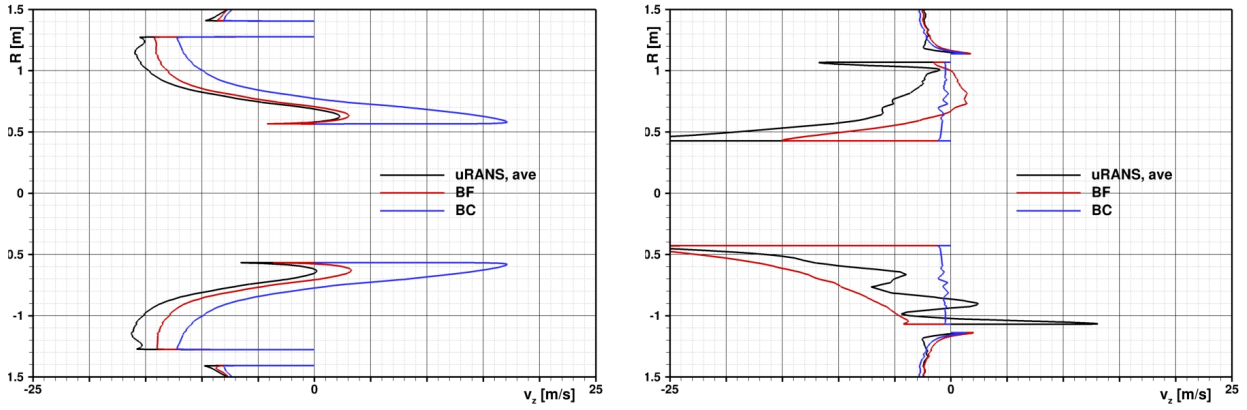

(a) Intake location (b) Nozzle location

Figure 14. Development of the swirl component of the velocity in the horizontal plane along the engine centerline

At the intake location, just upstream of the rotor, the engine boundary condition solution shows a z-velocity component, which is due to effect of the taper of the empennage on the flow. An increase in these velocity components is found at the intake location in both the mean uRANS and the body force results, with the latter showing magnitudes roughly between those seen in the boundary condition and mean uRANS results. This higher magnitude swirl in the mean unsteady simulaltion data most likely result from the periodic displacement effect introduced by the rotating blades, which cause an upstream swirl component in the intake flowfield for this case in addition to that seen in both of the other engine modeling approaches.

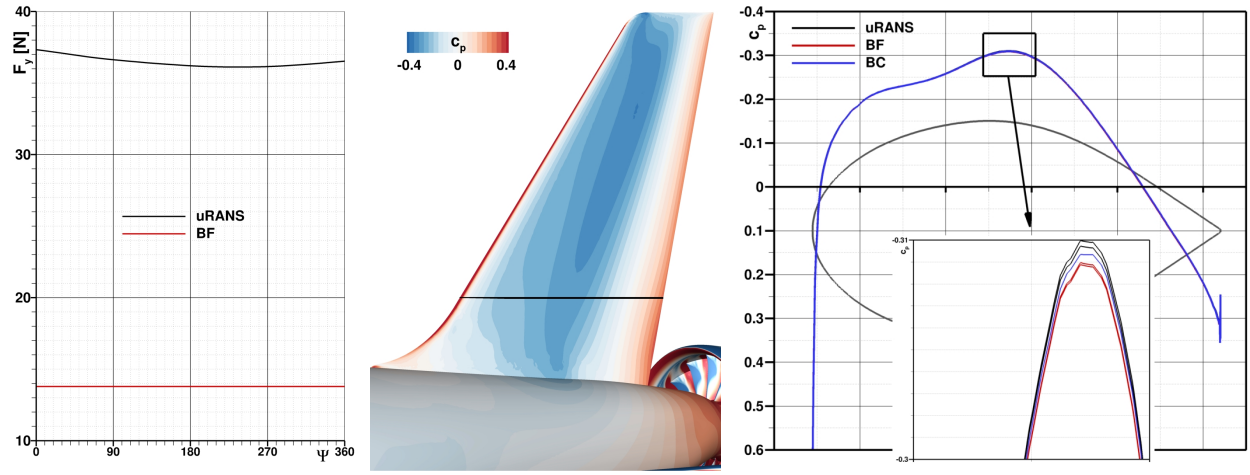

(a) VTP side force development during one rotor revolution (b) VTP pressure distribution contours (c) VTP section pressure distribution comparison for the three engine modeling approaches

Figure 15. Aft BLI propulsor impact on the vertical tailplane aerodynamics

The uRANS results show that this upstream swirl component form the rotating fan has an influence on the airframe in the immediate vicinity of the aft propulsor. Figure 15(a) compares the side force produced by the VTP as predicted in the uRANS and body force simulations. For the simulation with the boundary condition, no side force is predicted, thus it is not included in the figure. The uRANS results show a notably larger side force is generated by the VTP than when the BLI propulsor is modeled using the body force model. For a VTP section marked by the black line in figure 15(b), figure 15(c) compares the pressure distribution as computed in the simulations using the three different engine modeling approaches. Hardly any differences are evident at the scales used to show the complete sectional pressure distribution, which also indicates the expected symmetrical flow around the VTP at this non-sideslip cruise flight condition. However, the inset in figure 15(c), a zoom into the region of the minimum value of the pressure coefficient

at roughly the mid-chord positions shows subtle differences between the three simulation results. While the boundary condition-based CFD result retains the fully symmetric pressure distribution even at this scale, small differences between the left and right side of the VTP are discernible for the body force and most notably so for the uRANS simulations. The previous discussion of the swirl component of the velocity found in the intake in the case of the fully geometrically modeled rotor in the uRANS results is therefore thought to lead to a subtle increase in the asymmetry of the flow around the VTP versus the body force simulations, which in consequence results in an increased and potentially non-negligible side-force to be produced even at these non-sideslip flight conditions.

V. Conclusions and Outlook

An in-depth aerodynamic study of a complete transport aircraft configuration utilizing a boundary-layer ingesting aft propulsor was performed, culminating with a full unsteady simulation of a specifically designed aft BLI propulsor at the cruise flight condition. It was shown that mean performance predictions of the engine in the installed setting are not strongly dependent on the temporal resolution used in the uRANS approach, making a good prediction possible with relatively course time-steps at simulations run-times on the order of a few days. The accurate accounting of the unsteady flow features, in particular the interactions between the BLI propulsor rotor and stator, do necessitate a higher temporal resolution - which may be needed if an aeroacuostic analysis is done based on the CFD results or if detailed blade loading data is required for the structural design for example. Additionally, the BLI propulsor was also modeled using a medium-fidelity body force and a basic engine boundary condition approach. Comparisons showed that for most aspects relating to the external aerodynamics analysis all three approaches yielded broadly similar results, with the body force model in particular showing a very good match with the mean uRANS results in most of the critical evaluations of the flowfield. The paper discussed some aspects of the simulation approaches, as they relate to the fidelity and quality of the aerodynamic results, and gives an insight into the respective advantages and disadvantages. The uRANS approach was found to resolve additional upstream swirl effects in the intake of the BLI propulsor relating to the periodic passage and flow displacement effects introduced by the physically modeled blades of the rotor. This effect does have a small but non-negligible impact on the VTP in the direct vicinity of the propulsor, leading to a side force being generated even at the non-sideslip cruise flight conditions studied here.
A final BLI propulsor fan stage design, fully optimized for the non-uniform inflow conditions present for this fully installed case, will be investigated in the near future using the uRANS and body force approaches, and comparisons between the two distortion tolerant fan stage designs developed in the frame of this collaborative will be performed to further enhance the understanding of this promising propulsion-airframe integration scenario and help support both the engine and airframe design for these types of configurations.

VI. Acknowledgement

Airbus is greatly acknowledged for a fruitful collaboration on many aspects of BLI propulsion and for permitting publication of this work. Special thanks goes to William Thollet, who was an invaluable supporter of the work performed both on the airframe and the propulsion aspects in this collaboration.

References

[1]Welstead, J. and Felder, J. L., "Conceptual Design of a Single-Aisle Turboelectric Commercial Transport with Fuselage Boundary Layer Ingestion," *54th AIAA Aerospace Sciences Meeting*, San Diego, California, USA, January 2016.

[2]Plas, A., Crichton, D., Sargeant, M., Hynes, T., Greitzer, E., Hall, C., and Madani, V., "Performance of a Boundary Layer Ingesting (BLI) Propulsion System," *45th AIAA Aerospace Sciences Meeting and Exhibit*.

[3]SMITH, A. M. O. and ROBERTS, H. E., "The Jet Airplane Utilizing Boundary Layer Air for Propulsion," *Journal of the Aeronautical Sciences*, Vol. 14, No. 2, 1947, pp. 97–109.

[4]Smith, L. H., "Wake ingestion propulsion benefit," *Journal of Propulsion and Power*, Vol. 9, No. 1, 1993, pp. 74–82.

[5]Schnoes, M. and Nicke, E., "A Database of Optimal Airfoils for Axial Compressor Throughflow Design," *Proceedings of the GPPS 2018*, May 2018.

[6]Siller, U., Voß, C., and Nicke, E., "Automated Multidisciplinary Optimization of a Transonic Axial Compressor," 01 2009.

[7]Becker, K., Heitkamp, K., and Kügeler, E., "Recent Progress In A Hybrid-Grid CFD Solver For Turbomachinery Flows," *V European Conference on Computational Fluid Dynamics ECCOMAS CFD 2010*, edited by J. C. F. Pereira, A. Sequeira,

and J. M. C. Pereira, Juni 2010.

[8]Trost, M. and Spinner, S., "Design Optimization of a Rear Fuselage Fan for Different Boundary Layer Profiles," *20. Onera-DLR Aerospace Symposium (ODAS)*, Braunschweig, Germany, 2020.

[9]Gerhold, T., "Overview of the Hybrid Rans Code TAU," *MEGAFLOW - Numerical Flow Simulation for Aircraft Design, Notes on Numerical Fluid Mechanics and Multidisciplinary Design (NNFM)*, edited by N. Kroll and J. K. Fassbender, Vol. 89, Springer Berlin Heidelberg, Berlin, Heidelberg, 2005, pp. 81 – 92.

[10]Wilcox, D. C., "Reassessment of the scale-determining equation for advanced turbulence models," *AIAA Journal*, Vol. 26, No. 11, 1988, pp. 1299–1310.

[11]Menter, F.-R., "Two-Equation Eddy-Viscosity Turbulence Models for Engineering Applications," *AIAA Journal*, Vol. 32, No. 8, 1994, pp. 1598–1605.

[12]Jameson, A., "Time Dependent Calculations Using Multigrid, with Applications to Unsteady Flows Past Airfoils and Wings," *10th Computational Fluid Dynamics Conference*, No. AIAA 1991-1596, Honolulu, HI, USA, June 1991.

[13]Langer, S., Schwöppe, A., and Kroll, N., "The DLR Flow Solver TAU - Status and Recent Algorithmic Developments," *52nd Aerospace Sciences Meeting*, No. AIAA 2014-0080, National Harbor, MD, USA, Januar 2014.

[14]Spinner, S., Trost, M., and Schnell, R., "An Overview of High Fidelity CFD Engine Modeling," *AIAA SCITECH 2022 Forum*.

[15]Meinel, M. and Einarsson, G., "The FlowSimulator framework for massively parallel CFD applications," 06 2010.

[16]Hall, D. K., *Analysis of Civil Aircraft Propulsors with Boundary Layer Ingestion*, Ph.D. thesis, TU Braunschweig,Massachusetts Institute of Technology, 2015.

[17]Thollet, W., Dufour, G., Carbonneau, X., and Blanc, F., "Body-force modeling for aerodynamic analysis of air intake – fan interactions," *International Journal of Numerical Methods for Heat and Fluid Flow*, Vol. 26, 09 2016, pp. 2048–2065.

[18]Thollet, W., *Body force modeling of fan-airframe interactions*, Ph.D. thesis, University of Toulouse, 2017.

[19]Thollet, W., Dufour, G., Carbonneau, X., and Blanc, F., "Assessment of Body Force Methodologies for the Analysis of Intake-Fan Aerodynamic Interactions," *ASME Turbo Expo 2016*, Seoul, South Korea, 06 2016.

[20]Madrane, A., Heinrich, R., and Gerhold, T., "Implementation of the Chimera Method in the Unstructured Hybrid DLR Finite Volume TAU-Code," *6th Overset Composite Grid and Solution Technology Symposium*, Ft. Walton Beach, FL, USA, 2002, pp. 524–534.

[21]Madrane, A., Raichle, A., and Stuermer, A., "Parallel Implementation of a Dynamic Unstructured Chimera Method in the DLR Finite Volume TAU-Code," *12th Annual Conference of the CFD Society of Canada*, Ottawa, Ontario, Canada, 2004, pp. 524–534.

[22]Stuermer, A. and Akkermans, R., "Validation of Aerodynamic and Aeroacoustic Simulations of Contra-Rotating Open Rotors at Low-Speed Flight Conditions," *AIAA Aviation 2014*, No. AIAA 2014-3133, Atlanta, GA, USA, 2014.

[23]Stuermer, A., "DLR TAU-Code uRANS Turbofan Modeling for Aircraft Aerodynamics Investigations," *Aerospace*, Vol. 6, No. 11, 2019.

[24]Stuermer, A. W., "Validation of uRANS-Simulations of Contra-Rotating Open Rotor-Powered Aircraft at Take-Off Conditions," *AIAA Aerospace Sciences Meeting*, No. AIAA 2018-1265, Kissimmee, FL, USA, 2018.

[25]Stuermer, A., "Validation of Installation Effect Predictions Through Simulations of CRORs at Low-Speed Flight Conditions," *AIAA Aviation 2015*, No. AIAA 2015-2886, Dallas, TX, USA, 2015.